Available online at www.sciencedirect.com
ScienceDirect
Journal of the European Ceramic Society 29 (2009) 3363–3370
www.elsevier.com/locate/jeurceramsoc

Influence of green state processes on the sintering behaviour and the subsequent optical properties of spark plasma sintered alumina

Yann Aman [a,b,*], Vincent Garnier [a], Elisabeth Djurado [b]

[a] *Laboratoire MATEIS UMR CNRS 5510, Université de Lyon, INSA Lyon, 7 avenue Jean Capelle F-69621 Villeurbanne, France*
[b] *Laboratoire LEPMI UMR CNRS 5631, INP, Université Joseph Fourier Grenoble, Domaine Universitaire 1130 rue de la piscine, F-38402 Saint Martin d'Hères, France*

Received 15 February 2009; received in revised form 20 June 2009; accepted 14 July 2009
Available online 11 August 2009

Abstract

The present investigation gives a quantitative correlation between different green microstructures, and their sintering behaviour during spark plasma sintering. The green microstructures were elaborated via various green shaping processes such as direct casting and direct coagulation casting compared to uniaxial compaction of the as-received sub-micron grained corundum powder. Narrowing pore size distribution and reducing pore size (≈40 nm) in the green compact could favour cold densification during initial uniaxial pressing by grain sliding and rearrangement. This is attributed to the soft homogeneous touching network in direct-cast green samples. Consequently, grain growth was impeded and the onset of shrinkage was delayed. Moreover, the small pores and the narrow pore size distribution in the homogeneous green bodies led to higher final densities, with better optical properties compared to the less homogeneous green samples.
© 2009 Elsevier Ltd. All rights reserved.

Keywords: Al_2O_3; Shaping; Porosity; Spark plasma sintering; Optical properties

1. Introduction

Since a few years it has become possible to obtain fine and dense materials using the spark plasma sintering (SPS).[1,2] SPS is an emerging consolidation technique which combines pulsed electric currents and uniaxial compaction. Heating rates, applied uniaxial pressures and pulsed current patterns are the main factors responsible for the enhancement of densification kinetics and conservation of the sub-micron-scale structure of the materials.[3] Alumina is a common non-conductive ceramic material which has attracted the interest of some researchers in order to establish sintering models of spark plasma sintering technique.[4–6]

With a high optical band gap energy of 8.8 eV[7] corresponding to an absorption edge of ∼140 nm, pure single crystal of α-Al_2O_3 is transparent and colourless in the visible spectrum. The presence of pores (refractive index ≈1 versus 1.76 for corundum) is obviously unfavourable for light transmission properties. Thus, polycrystalline alumina (PCA) can be used in various optical applications like discharge lamps envelopes, optical windows or armors with the requirements of very low residual porosity, high temperature stability and durability, high mechanical strength and chemical durability.[8] This can be achieved with nearly fully dense PCA of sub-micron grain-size through HIP sintering of gel-casted corundum powders.[9] Light transmission properties of fine grained fully dense PCA can be described by a model based on Rayleigh-Gans-Debye approximation. This model proposed by Apetz and van Bruggen[10] predicts that high transparencies of PCA can be achieved by an accurate control of the grain size (<1 μm) and the porosity size (<100 nm) with a narrow distribution in the sintered microstructure. However, the uniform packing of particles at green state is a critical previous condition for the preparation of dense defect-free ceramics.[11] The sinterability of ultrapure sub-micron grained alumina powders is hindered by the agglomeration and the heterogeneous particle coordination in the green compacts. Green bodies with different states of agglomeration can locally induce differential shrinkage leading to abnormal grain growth.

* Corresponding author at: Laboratoire MATEIS UMR CNRS 5510, Université de Lyon, INSA Lyon, 7 avenue Jean Capelle F-69621 Villeurbanne, France. Tel.: +33 04 72 43 63 74; fax: +33 04 72 43 85 28.
E-mail address: yann.aman@insa-lyon.fr (Y. Aman).

0955-2219/$ – see front matter © 2009 Elsevier Ltd. All rights reserved.
doi:10.1016/j.jeurceramsoc.2009.07.014

During conventional or hot pressing sintering, such grain growth can be greatly influenced by the packing homogeneity and density of the green compacts.[12–14] Moreover, Krell and Klimke[15] have shown the influence of the porosity structure and distribution in colloidally prepared green bodies on the solid-state sintering of transparent alumina post-sintered with HIP.

In the literature, few researchers have investigated the spark plasma sintering of transparent ceramics.[16–21] In all cases, the powders were directly heated without any specific preparation. In Kim et al. papers,[19,20] transparent PCA was obtained by direct SPS-heating of the as-received sub-micron grained corundum powder without any pre-treatment or additives, whereas Jiang et al.[21] produced an optically transparent PCA in IR spectrum, with 0.2 wt% MgO added to the initial corundum powder. Thus, it is the objective of the present paper to highlight the critical importance of powder and green state processing through the investigation of the influence of different shaping processes and green state packing homogeneity on the sintering behaviour, the final microstructure and the subsequent optical properties through the spark plasma sintering of undoped polycrystalline alumina.

2. Experimental procedure

2.1. Green state processing and porosity

A high purity commercial corundum powder (BMA-15, >99.99% α-Al_2O_3, Baïkowski Chemicals, France) was used in the experiments. The as-received powder had an average particle size of 0.170 μm, a specific surface area of 14 m^2/g, as reported by the manufacturer. The powder was prepared by colloidal or dry routes using four different green shaping processes:

(A) The as-received alumina powder was directly dry-pressed in the SPS apparatus type HP D 25/1 (FCT Gmbh, Germany), under a constant uniaxial pressure of 80 MPa, without any treatment or additives.
(B) The powder was dispersed in an aqueous slurry with a solid content of 23 vol%, prepared at pH value of 3 in deionized water, with chlorhydric acid (HCl), followed by ultrasonification and magnetic agitation at 700 rpm for 1 h. The dispersed slurry was cast in a cylindrical mold (Ø 20 mm) on a porous support.
(C) The powder was well dispersed in an aqueous slurry with a solid content of 37 vol%, prepared at pH value of 10 in deionized water with an amount of ∼3 mol/cm^2 of 2-phosphonobutane-1,2,4-tricarboxilic acid (PBTCA, Lanxess-Bayer, France),[22] followed with ultrasonification and magnetic agitation at 700 rpm for 1 h. The dispersed slurry was also cast in a cylindrical mold (Ø 20 mm) on a porous support.
(D) The powder was dispersed in an aqueous slurry with a solid content of 47 vol%, prepared at pH of 10 in deionized water with an amount of ∼3 mol/cm^2 of PBTCA as dispersant, followed with ultrasonification and magnetic agitation at 700 rpm for 1 h. The slurry was prepared for the implementation of direct coagulation casting (DCC) process,[23] with the addition of aluminium acetate (C_2H_3AlOOH) as a coagulant agent, then cast in a non-porous cylindrical mold (Ø 20 mm), and placed in room steam at 55 °C for 1 h.

After 24 h-drying at room temperature, the green samples obtained from (C) and (D) were calcined in air at 750 °C during 10 h, in order to burn out the organic additive (PBTCA dispersant). In the following sections, those pre-treated samples will be respectively named (C′) and (D′). Porosity of green bodies was measured by mercury intrusion, using the equipment Autopore III (Micromeritics, Instr. Corp., USA). From the absolute porosities data, cumulative percent volumes, and pore size distributions were plotted to enable direct comparison of the results and evaluating porosity distributions.

2.2. Sintering, microstructure and optical transparency characterization

All the green samples were sintered in the SPS apparatus using the same cycle (applied uniaxial pressure of 80 MPa throughout the sintering cycle, heating rate of 8 °C/min, sintering temperature of 1300 °C, dwell duration of 60 min at 1300 °C, annealing at 1000 °C during 10 min and cooling at 120 °C/min). The temperature was controlled with a horizontal pyrometer focusing on a non-through hole closed at about 2 mm from the sample side in the graphite die. The total duration of the sintering cycle (heating rate, dwell, annealing, cooling) was less than 3 h.

The thermal expansion of SPS punches was determined through a dummy test and was used to correct the displacement data of the punches during SPS cycle. Then, the shrinkage $\Delta L/L_o$ during the constant heating rate step was determined using the expression $\Delta L = L_o - L$, with L_o the initial sample length and, L the instantaneous sample length determined by the monitored displacement of the graphite punches in the SPS.

Densities of sintered samples were evaluated using Archimede's method assuming a theoretical density (TD) of alumina of 3.987 g/cm^3. The immersion liquid was water at the temperature of 22 °C, with a density of 0.9978 g/cm^3. The balance method allowed a density precision of ±0.5%. Microstructural observations were achieved using SEM (JEOL 840, JEOL, Japan). Since it was difficult to observe precisely grains on thermally etched polished surfaces of spark plasma sintered alumina samples, fractures surfaces of samples were observed to determine grain sizes with the statistical correction factor 1.56.[24]

Apetz and van Bruggen[10] proposed the real in-line transmittance (RIT) as the real evaluation of transparency of sintered PCA, because it only takes in account the unscattered light through the sample (i.e. the real transmitted light). In this investigation, we only measured the in-line transmitted light as a function of the wavelength using a common commercial double beam spectrophotometer UV–visible light (PerkinElmer Lambda 35, USA). Strictly speaking, our measurements do not evaluate the transparency because of the large aperture of the incident beam. Indeed, with an opening angle in the range of 3–5°, one cannot exclude the scattered amounts from the mea-

sured intensity.[25] Nevertheless, this technique used in the present study is suitable for qualitative comparison of the optical scattering properties of the sintered samples. For this purpose, all the sintered specimens were polished both sides with a 0.500 μm diamond disk. The final thickness of samples ranged from of 0.80 to 1 mm.

3. Results and discussion

3.1. Porosity and pore size distribution in green bodies

The different shaping techniques (dry or colloidal process) resulted in different green densities and pore size-distribution. Fig. 1 shows the cumulative volume percentage of pore size distributions of the different samples. In this approach formerly proposed by Krell and Klimke,[15] pore size distributions are unified to 1 for each sample, independently of the total porosity which is quoted as an additional parameter. This enables direct comparison of the curves. From Fig. 1, whatever the green state process, pore sizes in all samples are lower than 100 nm, and in particular, pore sizes are lower than 50 nm for the colloidally prepared samples (B), (C) and (D). In the colloidal route samples, the dispersion efficiency and stability of the slurries mainly influenced the pores size distribution. The steepest slopes (i.e. narrowest distributions for samples C, D) are due to the beneficial effect of PBTCA dispersant. PBTCA promotes a ligand exchange process through its high affinity for Al^{3+} and enhanced adsorption of the dispersant at pH = 10 on alumina nanoparticles, as described by Liu et al.[22] The larger sizes of pores in (D) comparatively to (C) could be attributed to the direct coagulation casting process, in which well distributed hard agglomerates are produced during the controlled coagulation step, when ionic strength increases in the presence of the coagulation agent Al^{3+}.

Fig. 2 shows the pore size distribution as a function of pore diameter obtained from mercury incremental intrusion. From this figure, one can assume that the pore size distributions are normal. Large pore size distribution are observed in green compacts (A) and (B), whereas green compacts (C) and (D) are homogeneous. It is also worthnoting that after the calcination step at 750 °C during 10 h, the volume of pores calculated from the mercury intrusion (Table 1) slightly increased for sample (C′) and (D′). This slight increase in the pore intrusion volume can be attributed to the elimination of the organic dispersant in samples

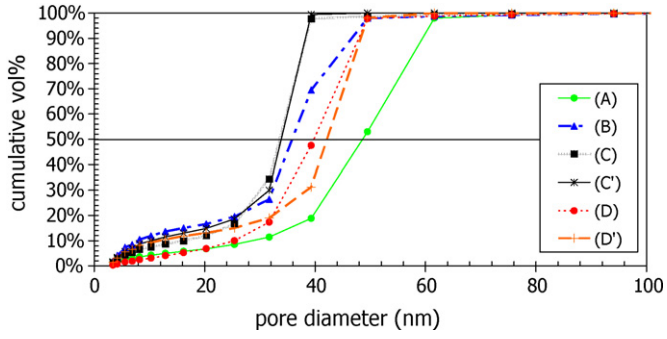

Fig. 1. Cumulative volume percentage of pore size distribution.

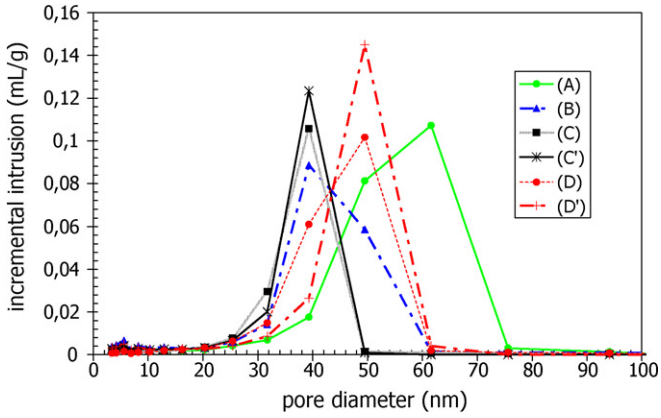

Fig. 2. Pore size distribution from mercury volume intrusion.

(C) and (D) during the calcination, since the content of organic dispersant in the initial slurry was approximately 1 vol%. It was accompanied with the decrease of the finest pores, which was clearly marked in the case of sample (D′). The elimination of the finest pores is probably due to the Ostwald ripening mechanism during the calcination stage, since matter transport could occur by surface diffusion and favour the elimination of the finest particles, as observed by Sato and Carry.[26] Consequently, it can be expected slightly lower green densities for these calcined samples but more homogeneous samples with smoother and more uniform continuous pore channel.[27]

From Table 1, a nearly linear relationship can be found between the most-frequent pores sizes (center of the lognormal distribution) and the green compacts densities. We note that the finer the most-frequent pore size is, the higher the green density is. This relationship seems independent of the consolidation technique, as also observed by Roosen and Bowen.[28] From Kozeny's equation[29] Eq. (1), one can express the green density in uniform compact to pore size as follows:

$$\frac{r_{\text{pore}}}{R_{\text{particle}}} = \frac{2}{3}\left(\frac{1-\rho_g}{\rho_g}\right) \quad (1)$$

In this equation, r_{pore} represents the most-frequent pore radius measured from mercury intrusion, R_{particle} is the surface area equivalent spherical particle radius, and ρ_g is the relative green density. Plotting the ratio $r_{\text{pore}}/R_{\text{particle}}$ (Eq. (1)) against the relative green density measured by mercury intrusion (Fig. 3) shows a good linear fitting dependence for the green samples before the compaction step. Higher green densities (C, B) are obtained for smaller ratio $r_{\text{pore}}/R_{\text{particle}}$ (0.44 and 0.46 respectively). Consequently, it is expected that a green shaping process that leads to finer most-frequent pore sizes in well dispersed green bodies would be more favourable to achieve higher green density.

Fig. 4 shows the axial linear shrinkage of each green sample during the cold compaction step in the SPS apparatus. Differences in shrinkage behaviour under cold uniaxial compaction are observed and could be attributed to the different states of agglomeration in the green bodies. Indeed, based on interparticle pairs potentials calculations, Franks and Lange[30] showed the link between consolidation behaviour at green state and slurry characteristics. In the case of well dispersed slurry (as sam-

Table 1
Samples characteristics before and after SPS.

Sample	Porosity (%)	Most-frequent pore size (nm)	Relative sintered density after SPS cycle (%)	Average grain size of SPS samples (μm)
(A)	50 ± 1.25	60	99.2	4.73
(B)	41 ± 1.47	40	99.9	3.78
(C)	40 ± 1.5	40	Not measured	Not measured
(C′)	42 ± 1.45	40	∼100	0.95
(D)	46 ± 1.35	50	Not measured	Not measured
(D′)	48 ± 1.3	50	99.3	0.88

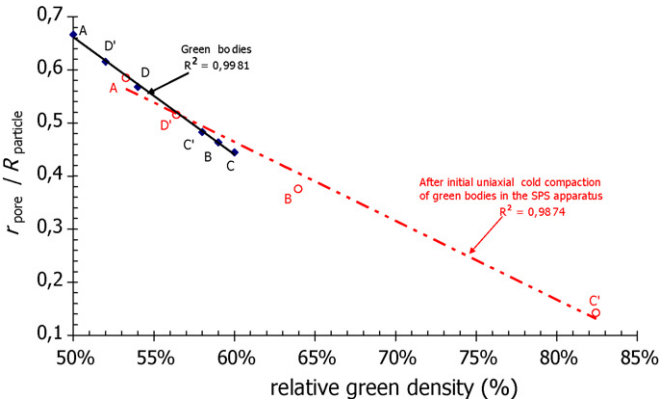

Fig. 3. Ratio pore size to surface area function green density.

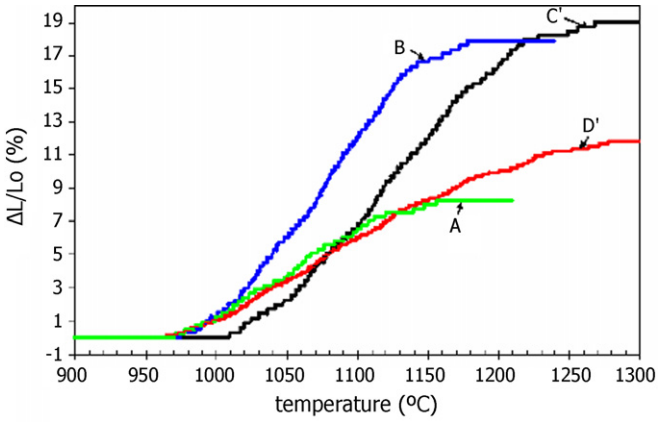

Fig. 5. Linear shrinkage at constant heating rate during SPS.

ple (C)), particles form a non-touching network due to strongly repulsive interparticle potentials. After direct casting and drying, particles form a soft homogeneous touching network. Thus, under uniaxial compaction, less pressure is required to push the soft touching particles in a manner to eliminate the larger voids, and allow grains sliding and rearrangement. This could explain the significant linear shrinkage of the sample (C′) after cold compaction in the SPS apparatus (Fig. 4). On the contrary, negligible shrinkage appears at high applied pressure for (D′), due to a stiffer network of agglomerates formed by particles after direct coagulation casting. Thus, increasing the homogeneity and dispersion state through green state process allowed to increase the packing density in the green body and favoured cold densification under SPS uniaxial pressure, probably by grain sliding and rearrangement. The calculated relative densities from the geometrical dimensions and shrinkage allowed to plot the ratio $r_{pore}/R_{particle}$ for the compacted green samples (Fig. 3). The applied cold uniaxial pressure (80 MPa) at the beginning of the SPS cycle had beneficial effect on increasing the green packing density and significantly reducing the pore size. This could lead, at the beginning of sintering, to early closure of an important fraction of remaining small pores in the homogeneous sample (C′).

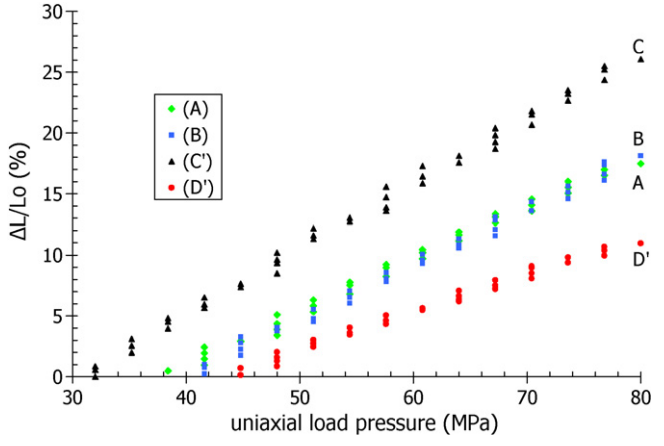

Fig. 4. Axial linear shrinkage at room T° under load pressure.

3.2. Sintering behaviour

3.2.1. Densification during constant heating rate (CHR)

Densifications kinetics during SPS sintering of the different consolidated samples were evaluated through the study of the linear shrinkage (Fig. 5) and shrinkage rate (Fig. 6) during the non-isothermal sintering stage. The figures were plotted in the temperature range from 900 to 1300 °C as the pressure remained constant throughout the constant heating rate step. The effect of pressure at room temperature was already mentioned in the previous section. Young and Cutler[31] showed that CHR method is extremely sensitive to the green compacts characteristics during initial sintering stage when the porosity is still open, provided that the heating rate is low.[32]

From Fig. 5, two different sintering behaviours can be distinguished. The onset of shrinkage for sample (A), (B) and (D′) started at 970 °C against 1010 °C for the well dispersed and homogeneous sample (C′). The onset of shrinkage is generally known as the starting of the intermediate stage of sintering, in which continuous and open pores channels at grains edges start to shrink.[33] In the previous section, it was shown that the grain

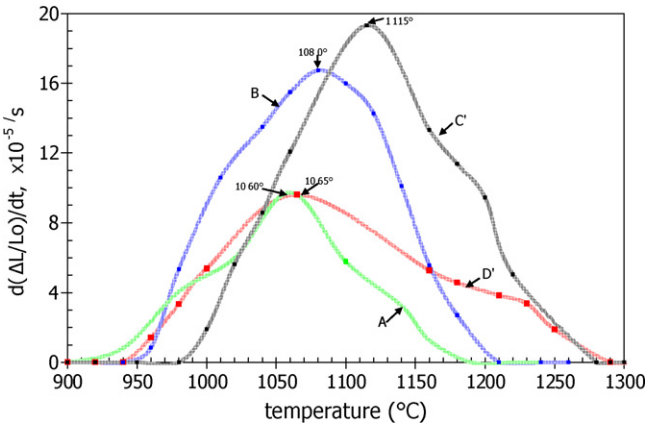

Fig. 6. Linear shrinkage rate at constant heating rate in SPS.

sliding and rearrangement in the homogeneous green compact (C′) led to a strong decrease of the pore to grain diameter ratio with increasing relative density under the cold uniaxial compaction in the SPS apparatus. This is assumed to favour the reduction of large interconnected pores volume. Because of the elimination of finest pores after calcination, and the decrease of large interconnected pores volume, the number of contacting particles around the interconnected pores (i.e. pore coordination number[34]) increased. This increase of pore coordination number could be thermodynamically favourable to the stability of pores as shown by Lange.[34] The shrinkage could be then delayed. Therefore, the subsequent grain growth that starts during the intermediate stage of sintering[14] is delayed.

Roosen and Bowen[28] showed that a much stronger dependence of shrinkage on pore structure is observed for the temperature at which the maximum of densification rate occurs. Fig. 6 shows the shrinkage rate, which is assumed to represent the linear densification behaviour of the different consolidated samples. Maximum shrinkage rate occurred at higher temperature for (C′) contrary to the other samples. This observation is contradictory to Roosen's work who found that decreasing pore diameter in the pore size distribution allows to reduce the temperature of maximum shrinkage rate in conventional sintering. This difference could be explained by the pores size, and also the width of the pore size distribution which was not evaluated in Roosen's work. Indeed, based on a lattice diffusion model, Zhao and Harmer[35] showed that narrowing pore size distribution initially limits grain growth and indirectly increases densification. During SPS, it is then expected that the narrow pore size distribution with small pores (<50 nm) in sample (C′) impedes the onset of grain growth during intermediate stage sintering, and favours densification by grain sliding under the applied uniaxial stress[36] until the coarsening mechanisms become predominant. Since the occurrence of a maximum linear shrinkage rates indicates a change of densification mechanism from sintering kinetics to coarsening ones as shown by Lange,[11] therefore it can be expected to have grain growth enhancement from this maximum shrinkage rate temperature.

From Fig. 6, the differences in curves shapes (flat or sharp peak) could be explained by the nature of agglomeration in the green compacts. From Li and Sun[37] work, fine and soft agglomerated corundum powder shrinkage rate curve presented a sharp peak (34.2×10^{-5}/s) at 1350 °C during pressureless sintering at CHR, compared to the hard agglomerated powders (15.6×10^{-5}/s) with a flat maximum. The shaping process (C) is assumed to allow the formation of green microstructures composed of a soft touching network of well dispersed particles that would shrink faster than the hard agglomerates in sample (D) due to the coagulation process. The lower experimental shrinkage rate values compared to Li's ones could be attributed to the

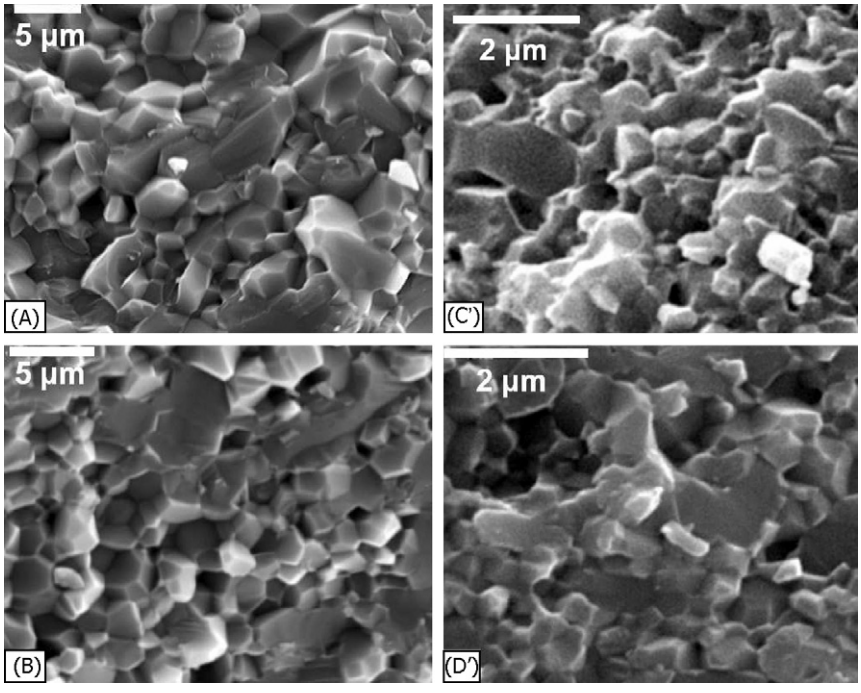

Fig. 7. SEM fractures surfaces micrographs of sintered samples.

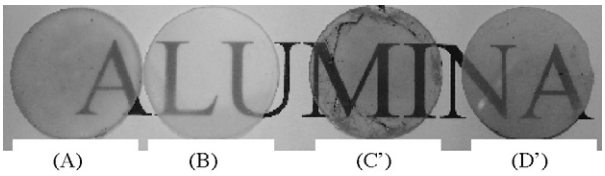

Fig. 8. Polished spark plasma sintered specimens.

different densification mechanisms and the enhancing effect of spark plasma sintering at lower temperatures.

3.2.2. Density and final microstructure characterization

The measured Archimede densities and grain sizes of sintered specimen are listed in Table 1. High density values are obtained for the colloidally prepared specimens. We also note that higher sintered densities are obtained for the higher green densities with smaller most-frequent pores size in the green bodies. Moreover, well dispersed and homogeneous green samples (C′, D′) allowed finer grains, probably due to grain growth inhibition in green compacts with narrow pore size distribution, as shown by Zhao and Harmer.[35]

3.3. Optical transmission properties of the spark plasma sintered samples

The different shaping techniques resulted in different optical transmission properties after spark plasma sintering. The polished specimens are shown in Fig. 8, and the measured in-line transmittances as a function of the incident wavelength are plotted in Fig. 9. As the polished specimens lie directly on the black fonts, one can say from Fig. 8 that sample (C′) is highly translucent whereas the other samples are translucent. This is also verified with the measured optical in-line transmittance in Fig. 9, which shows higher values for colloidally well-prepared samples (D′) and (C′). According to Apetz and van Bruggen,[10] the sources of light scattering in PCA are rough surfaces of polished samples, pores, grain boundaries (GB) and second phase (impurities) inclusions or precipitates. Since an amount of incident light is lost through multiple reflection/refraction or absorption when light meets the previous cited scattering centers, the in-line transmittance could be expressed as a Beer–Lambert's law:

$$T = (1 - R)^2 \exp(-\gamma d) \tag{2}$$

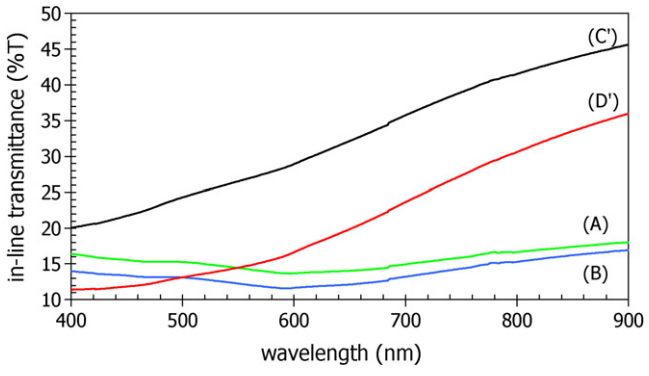

Fig. 9. In-line transmittance measurements.

Table 2
Real-in-line transmittance values calculated from Apetz.

Sample	RIT% calculated from Apetz model with the present study results $\lambda = 645$ nm, $d \approx 0{,}80$ mm	RIT% values from Apetz experiments with approximately same mean grain size $\lambda = 645$ nm, $d \approx 0{,}80$ mm
(C′)	40	38
(B)	4	7
Relative decrease	92%	84%

where R is the total reflectivity (~0.14), γ [m^{-1}] the total scattering (or absorption) coefficient and d [m] the sample thickness. During the spectrophotometer measurements, the incident wavelength is normal to the sample surfaces. Thus, with respect of a suitable reproducible polishing procedure, one could neglect the scattering of rough surfaces.[38] The total scattering coefficient (or absorption coefficient) is then determined by the contribution of each scattering center as follows:

$$\gamma_{sca} = \gamma_{pores} + \gamma_{GB} + \gamma_{impurities} \tag{3}$$

In Eq. (3), we could not neglect the contribution of impurities, since there is a weak yellow coloration of samples (C′, D′). This coloration can be attributed to graphite and/or carbon contamination as recently demonstrated by Bernard-Granger et al.[39] In the case of virtually pore-free sintered specimens (C′, B), since the mean grain radius r are lower than 10 μm (Table 1), the Rayleigh-Gans-Debye (RGD) approximation[10] can be applied at the incident wavelength in the medium of $\lambda_o = 645$ nm, and an average difference of refractive index $\langle \Delta n \rangle \sim 0.0053$. Thus, the real-in-line transmittance can be calculated as follows:

$$RIT = (1 - R)^2 \exp(-\gamma_{GB} d) \tag{4}$$

where,

$$\gamma_{GB} = \frac{3\pi^2 \Delta n^2 r}{\lambda o^2}$$

The comparative RIT values calculated from (4) for samples (C′) and (B) are presented in Table 2. These results agree well with Apetz's prediction of virtually pore free samples and show a strong influence of the grain growth on the transparency of the spark plasma sintered specimens when they are considered fully dense.

Plotting the scattering coefficient γ_{sca} (Fig. 10) against the inverse of wavelength square is more advantageous because γ_{sca} depends both on microstructural parameters independently of the sample thickness. Among those microstructural parameters, Pecharromàn et al.[40] have identified the grain size – in particular the maximum grain size – and a textural parameter. Fig. 10 highlights two different behaviours between the most homogeneous samples (C′, D′) compared to the less ones (A, B). In addition, three different scattering regimes could be distinguished: (a) for higher wavelengths, all the samples follow nearly the same dependence of λ^{-2}. According to Pecharromàn et al.,[40] this linear dependence law indicates a RGD scattering regime of grain scattering. (b) For the shortest wavelengths anomalous

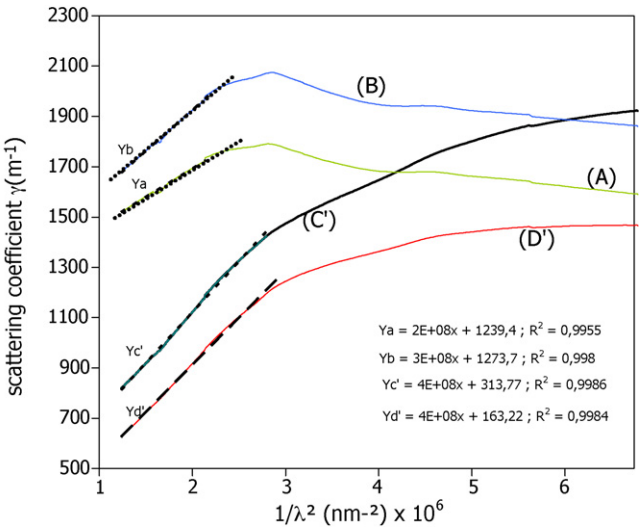

Fig. 10. Scattering coefficient vs. the inverse of wavelength square.

diffraction is assumed to saturate the scattering coefficient. (c) In between the two previous region, deviation from the linear law is attributed to grain with anomalous large size, with the probable contribution of residual pores. From the micrographs (Fig. 7), very few large grains can be observed in the finer sintered microstructures C′ or D′. This is attributed to the green shaping processing which allowed finer and homogeneous sintered microstructures. The differences in scattering behaviours between homogeneous samples and less ones, as shown in Fig. 10, clearly supports the importance of green shaping processing to achieve high transparency of spark plasma sintered PCA.

4. Conclusion

High translucencies of spark plasma sintered PCA can be achieved with an accurate control of grain growth, porosity and pore size distribution in the final sintered microstructures. The final microstructures are mainly influenced by the green shaping process which controls the homogeneity of particle packing, the tail of porosity, and pore size distribution in green compacts. In this study, it has been shown that narrowing pore size distribution and reducing the tail of pores (<50 nm) in green compacts delay the densification and consequently impede the onset of grain growth during the initial and intermediate stages of spark plasma sintering. A maximum linear shrinkage rates occurred at lower temperature during SPS compared to other conventional sintering performed with classical dilatometry. The change from sintering to coarsening kinetics at the maximum linear shrinkage during spark plasma sintering (at constant heating rate) could be delayed, due to the green compact homogeneity and state of agglomeration. Thus, the grain growth extent could be limited. It was also shown that samples with homogeneous green compacts and small most-frequent pore sizes can favour densification by grain sliding and rearrangement and lead to higher sintered density with SPS. Consequently, the optical properties of spark plasma sintered PCA can be strongly influenced by the sintered microstructures obtained from the different green shaped samples. Grain growth and heterogeneous grain size distribution can strongly decrease the optical transmission properties in spark plasma sintered samples.

The present investigation has shown that optical properties and more generally sintering behaviour of powders with SPS are mainly influenced by the green state homogeneity and pore size distribution. However, the influence of introduced impurities during colloidal processing may have an effect on the light transmittance by increasing the total scattering coefficient, or influencing the sintering mechanism during SPS. It should be interesting in further investigations to evaluate these impurities and their influence on sintering.

Acknowledgements

The authors gratefully acknowledge the “Région Rhône Alpes – MACODEV” for supporting this work, Pr. G. Fantozzi and G. Bonnefont from the SPS consortium at INSA Lyon.

References

1. Omori, M., Sintering, consolidation, reaction and crystal growth by spark plasma system (SPS). *Mater. Sci. Eng. A*, 2000, **287**, 183–188.
2. Jiang, D., Hulbert, D., Kuntz, J., Anselmi-Tamburini, U. and Mukherjee, A. K., Spark plasma sintering: a high strain rate low temperature forming tool for ceramics. *Mater. Sci. Eng. A*, 2007, **463**, 89–93.
3. Munir, Z. A., Anselmi-Tamburini, U. and Ohyanagi, M., The effect of electric field and pressure on the synthesis and consolidation of materials: a review of the spark plasma sintering method. *J. Mater. Sci.*, 2006, **41**, 763–777.
4. Shen, Z., Johnsson, M., Zhao, Z. and Nygren, M., Spark plasma sintering of alumina. *J. Am. Ceram. Soc.*, 2002, **85**(8), 1921–1927.
5. Wang, S. W., Chen, L. D. and Hirai, T., Densification of Al_2O_3 powder using spark plasma sintering. *J. Mater. Res.*, 2000, **15**(4).
6. Zhou, Y., Hirao, K., Yamauchi, Y. and Kanzaki, S., Densification and grain growth in pulse electric current sintering of alumina. *J. Eur. Ceram. Soc.*, 2004, **24**, 3465–3470.
7. French, R. H., Electronic band structure of Al_2O_3, with comparison to ALON and ALN. *J. Am. Ceram. Soc.*, 1990, **73**(3), 477–489.
8. Wei, G. C., Transparent ceramics for lighting. *J. Eur. Ceram. Soc.*, 2009, **29**(2), 237–244.
9. Krell, A., Blank, P., Ma, H., Hutzler, T., van Bruggen, M. P. B. and Apetz, R., Transparent sintered corundum with high hardness and strength. *J. Am. Ceram. Soc.*, 2003, **86**(1), 12–18.
10. Apetz, R. and van Bruggen, M. P. B., Transparent alumina: a light-scattering model. *J. Am. Ceram. Soc.*, 2003, **86**(3), 480–486.
11. Lange, F. F., Powder processing science and technology for increased reliability. *J. Am. Ceram. Soc.*, 1989, **72**(1), 3–15.
12. Xue, L. A. and Chen, L. W., Deformation and grain growth of low-temperature sintered high purity alumina. *J. Am. Ceram. Soc.*, 1990, **73**(11), 3518–3521.
13. Dynys, F. W. and Halloran, J. W., Influence of aggregates on sintering. *J. Am. Ceram. Soc.*, 1984, **67**(9), 596–601.
14. Cameron, C. P. and Raj, R., Grain growth transition during sintering of colloidally prepared alumina powder compacts. *J. Am. Ceram. Soc.*, 1988, **71**(12), 1031–1035.
15. Krell, A. and Klimke, J., Effects of the homogeneity of particle coordination on solid-state sintering of transparent alumina. *J. Am. Ceram. Soc.*, 2006, **89**(6), 1985–1992.
16. Chaim, R., Superfast densification of nanocrystalline oxide powders by spark plasma sintering. *J. Mater. Sci.*, 2006, **41**, 7862–7871.

17. Chaim, R., Marder-Jaeckel, R. and Shen, J. Z., Transparent YAG ceramics by surface softening of nanoparticles in spark plasma sintering. *Mater. Sci. Eng. A*, 2006, **429**, 74–78.
18. Kim, B. N., Hiraga, K., Morita, K. and Yoshida, H., Fabrication of transparent $MgAl_2O_4$ spinel polycrystal by spark plasma sintering processing. *Scripta Mater.*, 2008, **58**, 1114–1117.
19. Kim, B. N., Hiraga, K., Morita, K. and Yoshida, H., Spark plasma sintering of transparent alumina. *Scripta Mater.*, 2007, **57**, 607–610.
20. Kim, B. N., Hiraga, K., Morita, K. and Yoshida, H., Effects of heating rate on microstructure and transparency of spark plasma sintered alumina. *J. Eur. Ceram. Soc.*, 2009, **29**, 323–327.
21. Jiang, D., Hulbert, D. M., Anselmi-Tamburini, U., Ng, T., Land, D. and Mukherjee, A. K., Optically transparent polycrystalline Al_2O_3 produced by spark plasma sintering. *J. Am. Ceram. Soc.*, 2008, **91**(1), 151–154.
22. Liu, Y., Gao, L. and Guo, J., Comparative study on the stabilizing effect of 2-phosphonobutane-1,2,4-tricarboxilic acid and citric acid for alumina suspension. *Colloids Surfaces A: Physicochem. Eng. Asp.*, 2001, **193**, 187–195.
23. Pénard, A.-L., Rossignol, F., Nagaraja, H. S., Pagnoux, C. and Chartier, T., Dispersion of alpha-alumina powders using 2-phosphonobutane-1,2,4-tricarboxilic acid for the implementation of a DCC process. *J. Eur. Ceram. Soc.*, 2005, **25**, 1109–1118.
24. Mendelson, M. I., Average grain size in polycrystalline ceramics. *J. Am. Ceram. Soc.*, 1969, **52**(8), 443–446.
25. Krell, A., Huzler, T. and Klimke, J., Transmission physics and consequences for materials selection, manufacturing and applications. *J. Eur. Ceram. Soc.*, 2009, **29**, 207–221.
26. Sato, E. and Carry, C., Effect of powder granulometry and pre-treatment on sintering behavior of submicron-grained α-alumina. *J. Eur. Ceram. Soc.*, 1995, **15**, 9–16.
27. Lin, F. T., De Jonghe, L. C. and Rahaman, M. N., Microstructure refinement of sintered alumina by a two step sintering technique. *J. Am. Ceram. Soc.*, 1997, **80**(9), 2269–2277.
28. Roosen, A. and Bowen, H. K., Influence of various consolidation techniques on the green microstructure and sintering behavior of alumina powders. *J. Am. Ceram. Soc.*, 1988, **71**(11), 970–977.
29. Sweeney, S. M. and Mayo, M. J., Relation of pore size to green density: The Kozeny Equation. *J. Am. Ceram. Soc.*, 1999, **82**(7), 1931–1933.
30. Franks, G. V. and Lange, F. F., Plastic to brittle transition of saturated alumina powder compacts. *J. Am. Ceram. Soc.*, 1996, **79**(12), 3161–3168.
31. Young, W. S. and Cutler, I. B., Initial sintering with constant rates of heating. *J. Am. Ceram. Soc.*, 1970, **53**(12), 659–663.
32. Fang, T. T., Shiue, J.-T. and Shiau, F.-S., On the evaluation of the activation energy of sintering. *Mater. Chem. Phys.*, 2003, **80**, 108–113.
33. Coble, R. L., Sintering crystalline solids: I. Intermediate and final stage diffusion models. *J. Appl. Phys.*, 1961, **32**, 787–792.
34. Lange, F. F., Sinterability of agglomerated powders. *J. Am. Ceram. Soc.*, 1984, **67**(2), 83–89.
35. Zhao, J. and Harmer, M. P., Effect of pore distribution on microstructure development: I. Matrix pores. *J. Am. Ceram. Soc.*, 1988, **71**(2), 113–120.
36. Chaim, R., Densification mechanisms in spark plasma sintering of nanocrystalline ceramics. *Mater. Sci. Eng. A*, 2007, **443**, 25–32.
37. Li, J. G. and Sun, X., Synthesis and sintering behavior of nanocrystalline alpha-alumina powder. *Acta Mater.*, 2000, **48**, 3103–3112.
38. Kamei, A., Nakamura, A. M., Okamoto, H., Ishimoto, H. and Mukai, T., Measurements of light scattering by rough surfaces. *Adv. Space Res.*, 1997, **20**(8), 1609–1612.
39. Bernard-Granger, G., Benameur, N., Guizard, C. and Nygren, M., Influence of graphite contamination on the optical properties of transparent spinel obtained by spark plasma sintering. *Scripta Mater.*, 2009, **60**, 164–167.
40. Pecharromàn, C., Mata-Osoro, G., Antonio Dìaz, L., Torrecillas, R. and Moya, J. S., On the transparency of nanostructured alumina: Rayleigh-Gans model for anisotropic spheres. *Optics Express*, 2009, **17**(8), 6899–6912.